Optica Applicata, Vol. LVI, No. 1, 2026
DOI: 10.37190/oa/208835

Pipeline event recognition in distributed optical fiber acoustic sensing systems based on FMD

Junjie Zhang, Yong Kong*, Yuhao Liu, Xiaofan Tong, Xin Tang

School of Electronic and Electrical Engineering, Shanghai University of Engineering Science, Shanghai 201620, China

*Corresponding author: kkyy7757@163.com

To enhance the early warning rate of pipeline leak events and reduce the false alarm rate in Φ-OTDR -based DAS systems, this paper proposes a new method based on FMD. The introduced vibration event types include not only pipeline leaks but also hammer strikes, steel pipe hits, and noise. A 160-meter pipeline setup was constructed, and the sensing optical fiber wound around it was monitored to collect 2 240 samples. The results after denoising demonstrate the effectiveness of the proposed denoising method. Subsequently, features were extracted using overlapping frames, dimensionality reduction was performed with *t*-SNE, and after training with NRBO-XGBoost, the leak event recognition rate reached 99.74%, the average classification accuracy reached 98.71%, and the false alarm rate was reduced to 0.19%.

Keywords: pipeline leak, DAS, FMD, overlapping frames, NRBO-XGBoost.

1. Introduction

Pipeline leaks are an increasingly concerning issue, causing numerous severe incidents. Not only do they result in significant economic losses, but they also cause serious environmental damage and can even lead to explosions that threaten human lives.

Traditional manual supervision is inefficient and costly, while other commonly used methods of automated pipeline safety inspection include machine patrols and camera-assisted surveillance, but they often fail to achieve complete pipeline coverage and real-time monitoring [1]. However, in recent years, sensor technology has been advancing, and distributed fiber optic sensors have been widely used in the industrial field, combining it with pattern recognition technology to classify and identify leakage and other vibration events [2-6].

The traditional Φ-OTDR uses direct detection [7] to detect and localize signals by monitoring the variation of Rayleigh backscattered light (RBS) intensity in the sensing fiber. And the later coherent detection improves the signal-to-noise ratio and sensing range of Φ-OTDR. DAS is a new distributed fiber-optic sensing technology using coherent detection [8] developed on the basis of Φ-OTDR, which utilizes optical fiber as a transmission medium, and senses external environmental changes, such as acoustic and vibration signals, by detecting them and translating them into small changes in the sensing fiber. It has the characteristics of anti-electromagnetic interference, high sensitivity, can be measured over long distances, can be monitored in real time, and is resistant to harsh environments. It can be applied to pipeline leakage [9], oil detection [10], seismic survey [11], traffic safety [12] and so on. However, in practical engineering applications, the high sensitivity of the system makes it more likely to receive interference from interference sources, which results in it having a high interference alarm rate.

Therefore, signal denoising and feature extraction play a crucialrole in event recognition. In 1998, Dr. E. Huang proposed empirical mode decomposition (EMD) [13], which eliminates the need for selecting a window function or wavelet basis function, thus reducing recognition time. However, EMD is prone to mode mixing and residual noise issues for discontinuous signals and those with abrupt characteristics. To achieve better signal decomposition, variational mode decomposition (VMD) was introduced in 2014 [14]. Unlike the recursive filtering pattern of EMD [15], VMD iteratively searches for the optimal solution of the variational model, determining the center frequency and bandwidth of each modal component [16]. On the other hand, in 2023, feature mode decomposition (FMD) was proposed [17], which leverages the advantages of correlated kurtosis (CK) to consider both the impulsive and periodic characteristics of the signal [18]. This method iteratively updates the filter coefficients to construct an adaptive finite impulse response (FIR) filter, bringing the filtered signal closer to the inverse convolution accumulation target function, and uses an adaptive FIR filter bank to decompose the signal into different modes while assessing the impulsiveness and periodicity of the signal using the correlated kurtosis. Therefore, in order to further improve the denoising effect of DAS signals, as well as the recognition rate of vibration events, this paper selects FMD as the signal decomposition method and optimizes the selection of the number of its decomposition modes to denoise the acquired signals, and then extracts the feature vectors to classify and recognize them.

2. Principle

2.1. FMD

Feature mode decomposition (FMD) simultaneously considers the impulsive and periodic nature of signals, making it robust against noise and interference. It includes the design of FIR filter banks, filter updates, period estimation, mode selection, and feature mode decomposition. Let the initial signal of length N be denoted as $x(n)$. The FMD theory then becomes the problem of solving a constrained optimization problem, which is represented by the following equation:

$$\underset{\{f_k(l)\}}{\arg\max}\{\mathrm{CK}_M(u_k)\} = \frac{\sum_{n=1}^{N}\left(\prod_{m=0}^{M} u_k(n-mT_s)\right)^2}{\left(\sum_{n=1}^{N} u_k^2(n)\right)^{M+1}} \tag{1a}$$

$$\text{s.t.}\, u_k(n) = \sum_{l=1}^{L} f_k(l)x(n-l+1) \tag{1b}$$

where $u_k(n)$ denotes the k-th modal component, $\mathrm{CK}_M(u_k)$ represents the associated kurtosis, f_k denotes the k-th FIR filter with length L, T_s denotes the input period measured using the number of samples, and M denotes the order of the shift.

For the constrained problem in Eq. (1), an iterative eigenvalue decomposition algorithm is employed, and the decomposition is represented using the matrix in the following equation:

$$u_k = Xf_k \tag{2}$$

Where:

$$u_k = \begin{bmatrix} u_k(1) \\ \vdots \\ u_k(N-L+1) \end{bmatrix}$$

$$X = \begin{bmatrix} x(1) & \cdots & x(L) \\ \vdots & \ddots & \vdots \\ x(N-L+1) & \cdots & x(N) \end{bmatrix}$$

$$f_k = \begin{bmatrix} f_k(1) \\ \vdots \\ f_k(L) \end{bmatrix}$$

Therefore, the decomposition modes can be defined as:

$$\mathrm{CK}_M(u_k) = \frac{u_k^{(H)} W_M u_k}{u_k^{(H)} u_k} \tag{3}$$

The superscript H denotes the conjugate transpose operation, and W_M is used as an intermediate variable to control the weighted correlation matrix. Substituting Eq. (3) into Eq. (2), and after calculation, we obtain:

$$\mathrm{CK}_M(u_k) = \frac{f_k^{(H)} X^{(H)} W_M X f_k}{f_k^{(H)} X^{(H)} X f_k} = \frac{f_k^{(H)} R_{XWX} f_k}{f_k^{(H)} R_{XX} u f_k} \tag{4}$$

where R_{XWX} and R_{XX} are the weighted correlation matrix and the correlation matrix, respectively. Maximizing Eq. (4) with respect to the filter coefficients is equivalent to finding the eigenvector associated with the maximum eigenvalue λ of the following generalized eigenvalue problem:

$$R_{XWX} f_k = R_{XX} f_k \lambda \tag{5}$$

Through repeated iterative calculations, the k-th filter coefficient is updated using the solution of Eq. (5), bringing it closer to the target, which is the filter signal with the maximum associated kurtosis (CK).

The final determined modes will contain specific components of the original signal. FMD only selects the mode with the maximum CK value. To eliminate mode mixing or redundant modes, the mode with the highest correlation coefficient is locked, as a higher correlation coefficient indicates that the two modes contain more similar components [19].

2.2. NRBO

The Newton–Raphson-based optimizer (NRBO)[20] is a metaheuristic optimization algorithm proposed by SOWMYA *et al.* in 2024. NRBO uses the Newton–Raphson search rule (NRSR) and the trap avoidance operator (TAO), and employs several sets of matrices to further explore the optimal results. The NRSR enhances the convergence speed to achieve improved search space positions, while the TAO helps NRBO avoid local optima traps. The algorithm steps are as follows.

For example, for the n-th individual in the t-th iteration, the new individual expressions are:

$$x_n^{t+1} = r\left[rX_n^t + (1-r)X'^t_n\right] + (1-r)X''^t_n \tag{6}$$

$$X''^t_n = x_n^t - \delta \times (X'^t_n - X_n^t) \tag{7}$$

where x_n^t denotes the current position, x_n^{t+1} denotes the new position found using the NRSR rule, n denotes the individual index, r denotes a random number between 0 and 1, δ denotes adaptive coefficient, X_n^t and X'^t_n represent the newly derived vector positions obtained through updates of the current position and current optimal position, respectively.

3. Experiment

3.1. Signal acquistition

The experimental system is shown in Fig. 1. The sensing system used in this experiment is based on Φ-OTDR DAS. The system employs a narrow linewidth laser (NLL) with a linewidth of 3 kHz and an output power of 10 mW. The laser light is split into two beams by a 90:10 optical coupler (OC1), with 90% of the light serving as the probe light and 10% as the local oscillator light. The probe light is modulated by an acousto-optic modulator (AOM) with a bandwidth of 150 MHz to form pulse light. The modulated pulse light is then amplified by an erbium-doped fiber amplifier (EDFA) with a gain of 27 dB. The amplified pulse light is directed into the sensing fiber (SF) via an optical circulator (Cir). The Rayleigh backscattered light (RBS) from SF interferes with the local oscillator light at the second optical coupler (OC2), generating a beat frequency signal. This beat frequency signal is detected by a balanced photodetector (BPD) with a bandwidth of 200 MHz and collected using a data acquisition card (DAQ). The trigger pulse is provided by a pulse generator (PG) with a pulse repetition frequency of 20 kHz.

The data used in this study were collected from an experimental setup established in collaboration with Shanghai Ruiyi Environmental Technology Co., Ltd. The experimental system consists of a 160-meter-long water pipe that is vertically folded and contains four internal pipes: two steel pipes and two wooden pipes. Each pipe is wrapped with optical fibers, and small holes are randomly drilled at various positions along the pipes to simulate leaking pipes. When water flows through the pipes, leakage occurs at these holes, and the resulting abnormal vibrations are captured by the optical fibers, allowing for leak detection and the issuance of an alert.

The core objective of this project is to improve the detection rate of leakage events and reduce the false alarm rate. However, focusing solely on leakage events and noise does not provide a comprehensive solution, as real-world applications may be affected

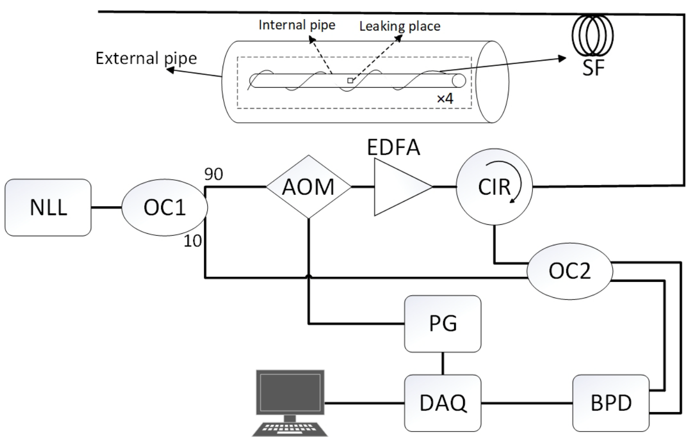

Fig. 1. Experimental structure diagram.

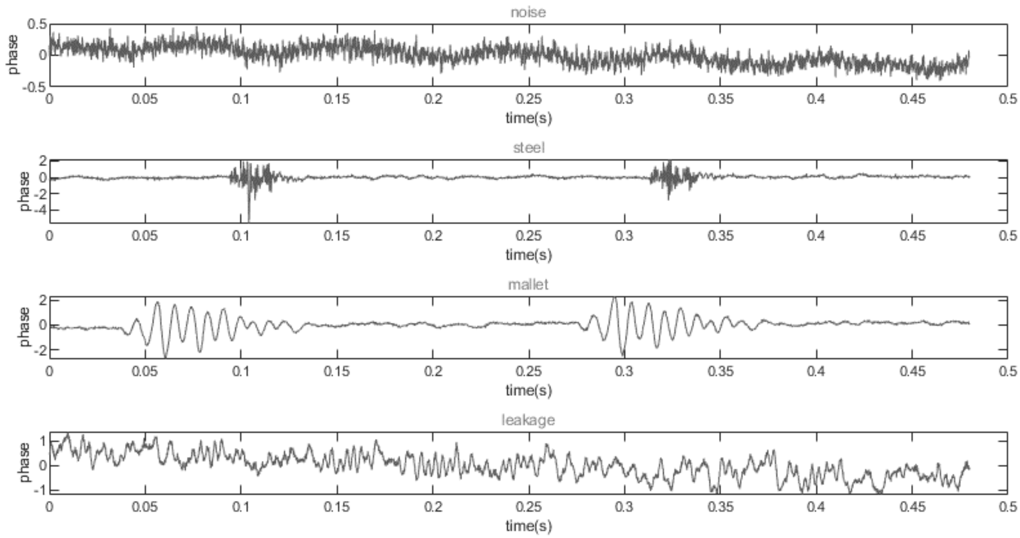

Fig. 2. Four vibration signals.

by other abnormal vibrations and human interference. Therefore, two additional events (steel tube tapping and wooden hammer tapping) have been included. The tapping positions coincide with the pipe leakage holes, located approximately 78 meters along the pipe. The data acquisition system divides the 160-meter-long pipe into 40 channels, with each channel covering a 4-meter segment. Consequently, the signal of interest can be extracted from the 20th channel. The four types of vibration signals, each consisting of 3840 sampling points (with a duration of 0.48 seconds), are shown in Fig. 2.

The analysis reveals that the noise signal exhibits a sinusoidal waveform and has a certain periodicity. The signal from the steel tube tapping is more concentrated at the tapping points, while the signal from the wooden hammer tapping is more dispersed at the tapping points. The reason for this difference is likely that the deformation of the pipe caused by the steel tube results in higher-frequency vibrations compared to the wooden hammer. The leakage signal, on the other hand, does not have a fixed shape and is relatively chaotic, making it difficult to identify any regular pattern.

3.2. Signal denoising

In the process of modal decomposition and denoising of the collected signals, the selection of modal components is a crucial step. If the selection is inappropriate, modal aliasing can occur regardless of the modal decomposition method used. Relying on manual experience for this process is also inefficient. Therefore, this paper combines PSO with FMD. PSO evaluates the signal based on seven criteria: envelope entropy, envelope spectrum kurtosis, amplitude spectrum entropy, fuzzy entropy, sample entropy, permutation entropy and information entropy. It then determines the optimal number of decomposed modes k, allowing for an adaptive selection of the number of decomposed modal components, thus processing the signals more efficiently.

For example, Fig. 3(a) shows a type of wooden hammer signal. First, the signal is analyzed using PSO with a particle count of 3, which determines $k = 4$. This means that the signal is decomposed into 4 modal components, which will have the least modal aliasing, making it more conducive to subsequent signal reconstruction. Therefore, the

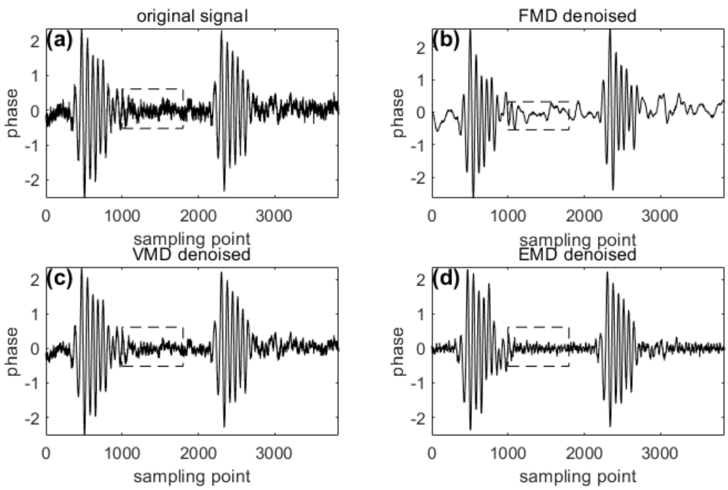

Fig. 3. Comparison of three denoising methods for mallet tapping signal. (a) The original signal; (b) FMD denoising; (c) VMD denoising; (d) EMD denoising.

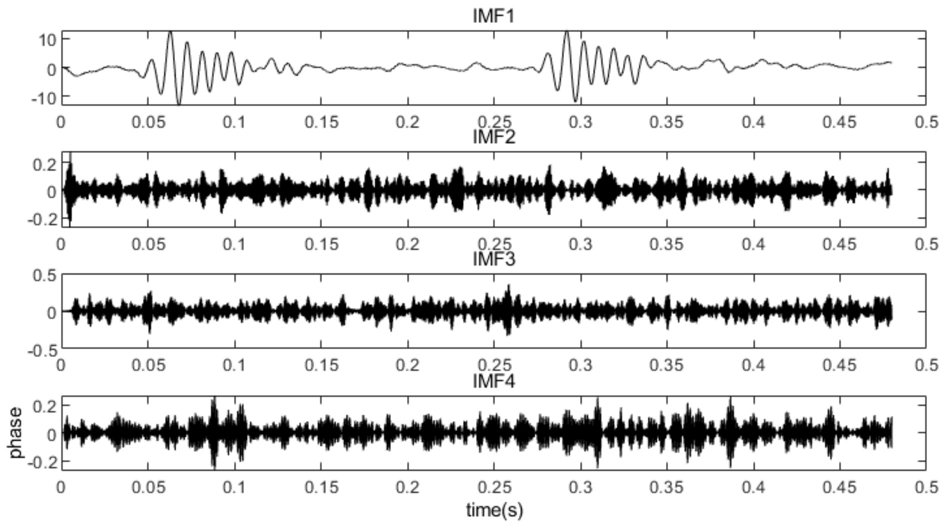

Fig. 4. The time-domain graphs of the four modal components obtained through FMD decomposition.

FMD algorithm is used to decompose the signal into 4 IMF components. The time-domain plots of the IMF components are shown in Fig. 4. Generally, the effective signal is primarily present in the low-frequency components, and the content of the figure confirms this. To evaluate the similarity of signals, we typically use the Pearson correlation coefficient (PCC), IMF1 contains the clearest mallet strike signal. After calculation, the PCC between IMF1 and the original signal is 0.7867, while the PCC values for the other four components are 0.0024, 0.0043 and 0.0035, respectively. By performing a fast Fourier transform (FFT) on each time-domain component, the frequency-domain plots shown in Fig. 5 are obtained. It is evident that the modal components increase gradually from frequency bands 1 to 4, with no modal aliasing, and the separation is very distinct. As for distinguishing effective components, relying solely on manual differentiation is highly inefficient. Therefore, the average of the maximum and minimum PCC between IMFs is calculated and used as a threshold. Components with PCC values greater than this threshold are considered effective. By synthesizing all the effective components, a denoised reconstructed signal is obtained, as shown in Fig. 3(b). In the dashed box, it is clearly visible that the impact of the mallet strike on the phase has significantly decreased. The denoising effects of the currently popular VMD and EMD methods are shown in Fig. 3(c) and (d), respectively. Compared to FMD, the denoising effects within the dashed box are less effective. In addition to the mallet signal, the denoising effects of the steel tube tapping signal and the leakage signal after FMD decomposition are also shown in Fig. 6. From the perspective of feature extraction, the more distinct and prominent components in the signal are emphasized, making

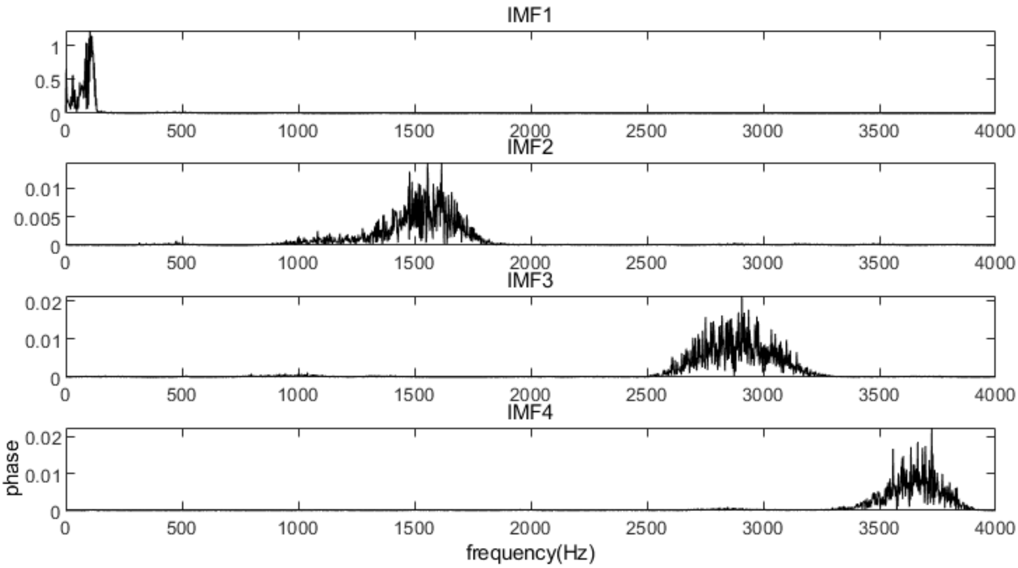

Fig. 5. The frequency-domain graphs of the four modal components obtained through FMD decomposition.

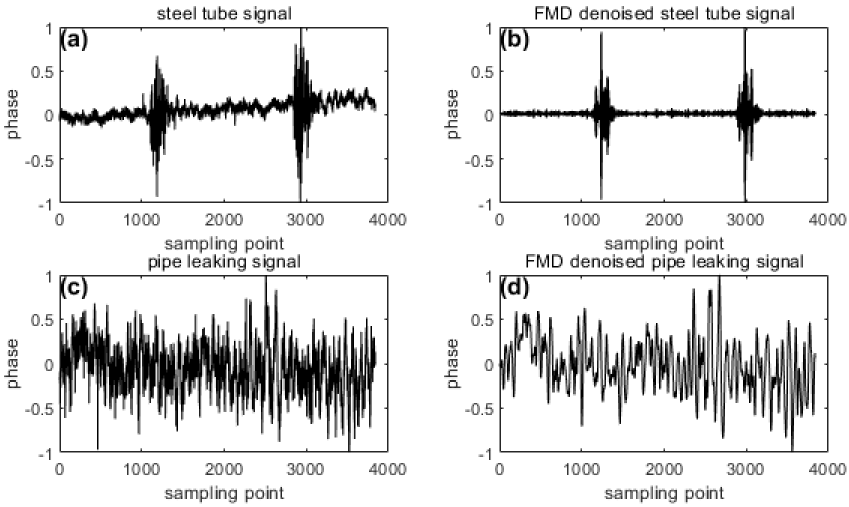

Fig. 6. Comparison of three denoising methods for mallet tapping signal. (a) The original steel tube signal; (b) FMD denoised steel tube signal; (c) the original leakage signal; (d) FMD denoised leakage signal.

the extracted feature vectors more valuable. Therefore, FMD is chosen as the decomposition method in this study.

3.3. Feature selection and extraction

Next, we proceed with feature extraction. The traditional method involves cutting the signal into equal segments. Taking the steel tube tapping signal as an example, we set the frame length to 480 sampling points, which results in 8 frames for each signal, as shown in Fig. 7. Although the second steel tube tapping waveform is well captured in frame f5, the transition between frames f1 and f2 cuts the first steel tube vibration waveform, making it easy to mistakenly interpret it as a noise-like feature during the feature extraction process, thereby affecting recognition accuracy.

Therefore, we use an overlapping frame method for feature extraction. The frame length is set to 960 sampling points, and each frame is shifted forward by 480 sampling

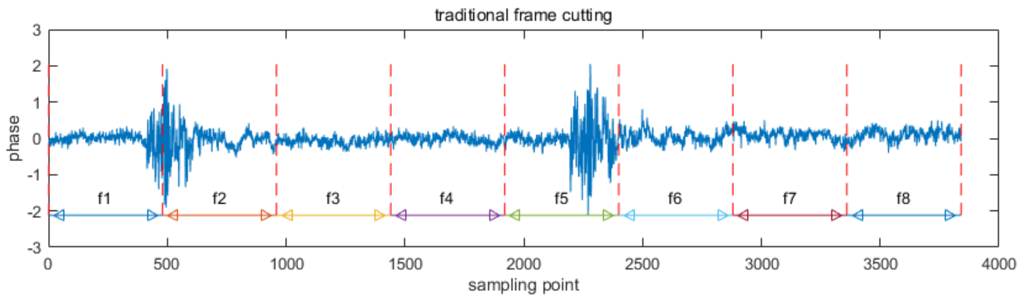

Fig. 7. Cutting frame feature extraction method.

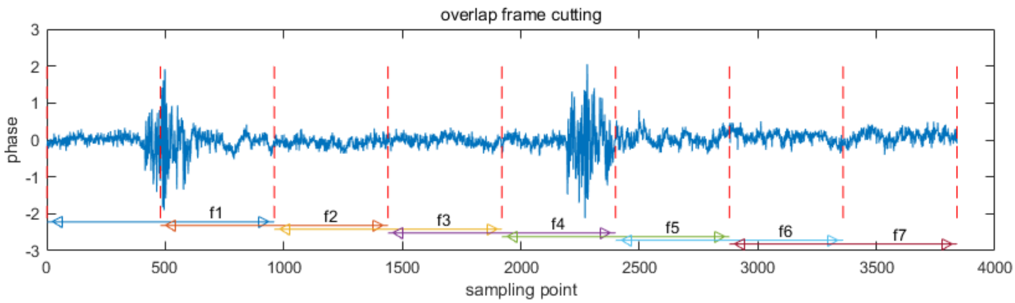

Fig. 8. Overlapping frame feature extraction method.

points to form the next frame, as shown in Fig. 8. This way, both f1 and f5 can effectively capture the key vibration information.

Next, we calculate the short-time energy, short-time zero-crossing rate, kurtosis and skewness for each frame as features.

Short-time energy reflects the signal's strength or power but is easily affected by noise. The short-time zero-crossing rate indicates the number of times the signal crosses zero in a short period, which reflects the frequency characteristics of the signal. Kurtosis is a measure of the sharpness of the signal's distribution, representing the shape of the data distribution. Since one signal is divided into 7 frames, after the calculation, each signal will have 21 features extracted, which are then combined into a feature vector. The visualization results of each feature vector are presented in Fig. 8.

3.4. Feature dimension reduction

In classification and recognition, if there are too many features, it often increases the model's complexity and training time. Furthermore, as shown in the previous feature extraction steps, different signal events often share "redundant frames", meaning that some frames only contain noise. To reduce their impact on the model's recognition accuracy, it is necessary to perform dimensionality reduction. We use the t-SNE dimensionality reduction method to reduce the original 7 features of each feature vector to 2 features. Thus, each event is described by 6 features in total.

The visualization of the dimensionality reduction process is presented in Fig. 9. As observed: (a) the short-time energy effectively discriminates between noise and leakage signals, though the mallet and steel tube impact signals exhibit partial overlap; (b) the short-time zero-crossing rate distinctly separates mallet impacts, whereas (c) the kurtosis feature demonstrates poor separability between noise and leakage signals with complete overlap, while maintaining limited discriminative capability for mallet versus steel tube signals. Furthermore, several other features were ultimately excluded after experimental evaluation, such as the skewness shown in (d). Although skewness effectively characterizes the asymmetry of data distributions, it exhibited insufficient discriminative power for our pipeline vibration dataset. Forcible inclusion of such fea-

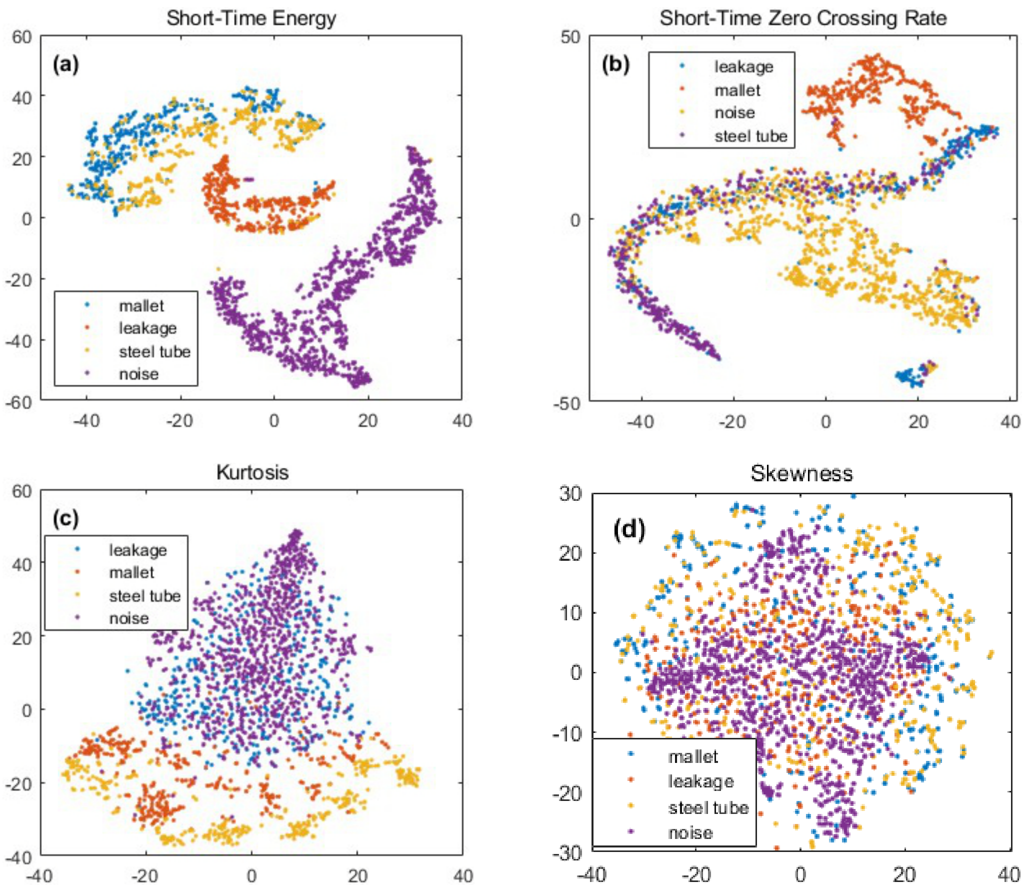

Fig. 9. The t-SNE dimensionality reduction results of the four feature vectors. (a) Short-time energy; (b) short-time zero crossing rate; (c) kurtosis; (d) skewness.

tures would not only introduce unnecessary computational complexity but also fail to enhance classification performance.

3.5. Pattern recognition

This study selected a total of 2 240 samples, which were categorized and documented in Table 1. To enhance the robustness and reliability of the results, we implemented a 5-fold cross-validation scheme during the training process. The dataset was randomly partitioned into five mutually exclusive subsets. For each validation round, four folds

T a b l e 1. The number of datasets.

Data	Leakage	Steel tube	Mallet	Noise	Totality
Amount	380	415	400	1045	2240

(80% of the data) served as the training set, while the remaining fold (20%) functioned as the validation set. This procedure was repeated five times to ensure each subset was used exactly once for validation, with the final performance metrics calculated as the average across all five validation results. The partitioned data was subsequently fed into the NRBO algorithm to determine the optimal parameter configuration for XGBoost. The NRBO was configured with 100 iterations, where the lower bound (lb) of the optimized parameters was set to [10, 001, 0.01] (maximum iterations, tree depth, and learning rate), and the upper bound (ub) was defined as [50, 012, 0.30]. This parameter range ensured sufficient convergence time during optimization while allowing exploration of a broader hyperparameter space. To balance computational efficiency and convergence speed, the population size for parallel processing was set to pop = 6.

The corresponding fitness curve is illustrated in Fig. 10, which clearly demonstrates the evolutionary trajectory of fitness values across iterations. The optimization process achieved convergence at the 17th iteration, yielding the optimal XGBoost parameters as follows: maximum iterations = 39, tree depth = 12, and learning rate = 0.2907. Figure 11 presents the classification performance of the optimized XGBoost model across all validation folds in the 5-fold cross-validation scheme, achieving a mean accuracy of 97.81% with minimal variance, indicating robust classification stability. The confusion matrix in Fig. 12 provides comprehensive classification results for in-depth analysis. Experimental results reveal certain misclassification phenomena between mallet strikes and steel pipe impacts, potentially attributable to controlled variations in impact force and striking methodology during data collection. Notably, the model demonstrates exceptional performance in leakage signal identification with 99.7% ac-

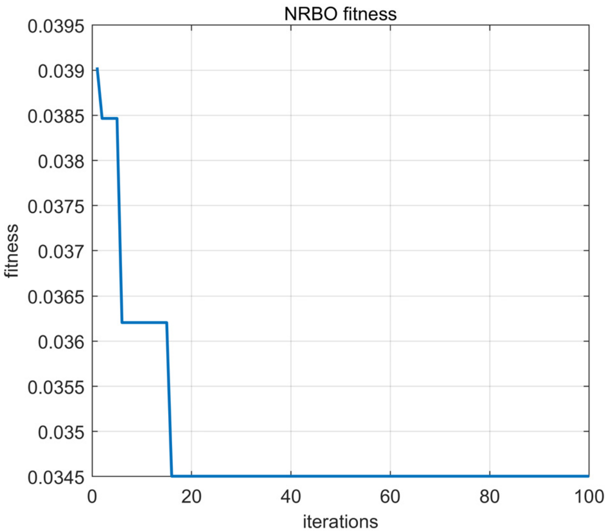

Fig. 10. NRBO fitness variation.

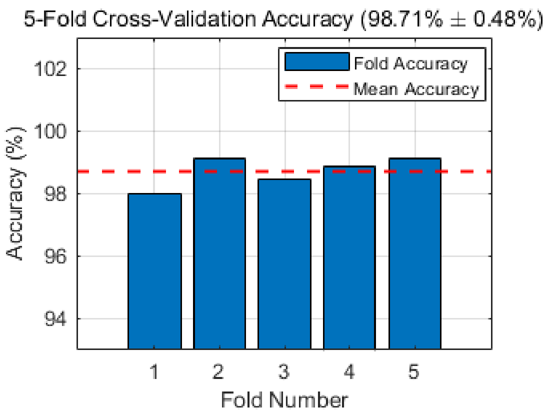

Fig. 11. The accuracy results from 5-fold cross-validation.

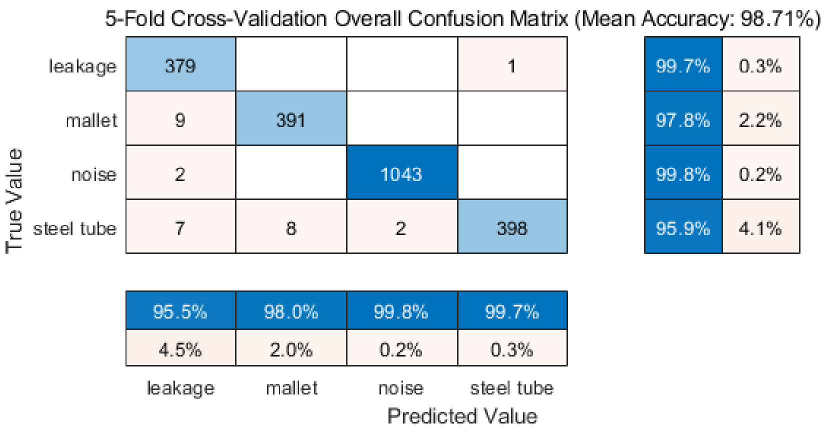

Fig. 12. Aggregated confusion matrix from the validation sets of 5-fold cross-validation.

curacy. For noise signals, the model achieves 99.8% recognition accuracy with a corresponding false positive rate of 0.2%, exhibiting strong discriminative capability.

For comparison, Table 2 presents classification results of four conventional models and XGBoost with default parameters (maximum iterations = 20, tree depth = 10, learning rate = 0.1) alongside three parameter-optimized XGBoost under identical experimental conditions. The analysis demonstrates that NRBO-XGBoost achieves the highest average recognition rate and lowest false alarm rate for pipeline signals. Among other models, both random forest (RF) and long short-term memory (LSTM) perform well with average recognition rates exceeding 95%, while support vector machine (SVM) shows poorer performance. Radial basis function neural network (RBFNN) shares SVM's limitation in accurately identifying steel pipe signals. The default XGBoost configuration already exhibits high recognition accuracy and fast computa-

Table 2. The recognition effect of the five methods.

Recognition rate	Leakage	Mallet	Noise	Steel tube	Average recognition rate	Recognition time [s/sample]	False alarm rate
RF	98.42%	95.50%	99.23%	86.75%	96.12%	0.025	0.77%
SVM	82.89%	65.00%	96.08%	75.90%	84.55%	0.029	3.92%
RBFNN	91.58%	90.00%	99.43%	78.55%	92.55%	0.034	0.57%
LSTM	95.26%	92.00%	98.47%	93.01%	95.76%	0.058	1.53%
XGBoost	97.63%	93.75%	99.52%	89.40%	96.29%	0.016	0.48%
SSA-XGBoost	96.05%	96.00%	98.85%	94.22%	97.01%	0.029	1.15%
ABC-XGBoost	98.42%	96.75%	99.52%	93.73%	97.77%	0.044	0.48%
NRBO-XGBoost	99.74%	97.75%	99.81%	95.90%	98.71%	0.024	0.19%

tion speed, motivating parameter optimization for further improvement. Ultimately, NRBO demonstrates superior performance, showing faster speed, lower false alarm rate, and accuracy improvements of 1.70% and 0.94% compared to sparrow search algorithm (SSA) and artificial bee colony (ABC) algorithm, respectively.

4. Conclusion

In this study, we built and collected pipeline leakage signals, and proposed the PSO-FMD method to denoise the signals collected by the DAS system, highlighting time-domain features. After extracting short-time energy, short-time zero-crossing rate, and kurtosis as feature vectors using the overlapping frame method, the data was input into NRBO -XGBoost for classification training. The final result achieved an average recognition rate of 98.71%, with a recognition rate of 99.7% for leakage events and a false alarm rate of 0.19%. This indicates that the proposed method is effective for identifying different vibration events, with a relatively low false alarm rate. However, the number of samples and types of interference in this experiment are still limited, and in the future, the sample size should be expanded to improve the model's robustness.

Acknowledgements
This work was supported in part by the Natural Science Foundation of China under Grant 62201338 and Natural Science Foundation of Shanghai under Grant 25ZR1402180.

References

[1] LI J., WANG Y., WANG P., BAI Q., GAO Y., ZHANG H., JIN B., *Pattern recognition for distributed optical fiber vibration sensing: A review*, IEEE Sensors Journal, **21**(10), 2021: 11983-11998. https://doi.org/10.1109/JSEN.2021.3066037

[2] HU X., DAI J.Y., WEI Z.Y., SHEN W., YU H., WU H.Y., XU Y.W., HU C.Y., DENG C.L., HUANG Y., *Markov transition fields and auto-encoder-based preprocessing for event recognition of Φ-OTDR*, Optica Applicata, **54**(2), 2024: 217-229. https://doi.org/10.37190/oa240208

[3] SHI Y., DAI S., LIU X., ZHANG Y., WU X., JIANG T., *Event recognition method based on dual-augmentation for a Φ-OTDR system with a few training samples*, Optics Express, **30**(17), 2022: 31232-31243. https://doi.org/10.1364/OE.468779

[4] SHI Y., LIU H., ZHANG W., CHENG Z., CHEN J., SUN Q., *Event recognition method based on feature synthesizing for a zero-shot intelligent distributed optical fiber sensor*, Optics Express, **32**(5), 2024: 8321-8334. https://doi.org/10.1364/OE.514878

[5] HU X., DONG H., KONG Y., YANG H., ZHANG D., *Effective zero-shot learning method for event classification in Φ-OTDR sensing systems*, Optics Express, **32**(20), 2024: 35495-35512. https://doi.org/10.1364/OE.537940

[6] GAN J., XIAO Y., ZHANG A., *Fused feature extract method for Φ-OTDR event recognition based on VGGish transfer learning*, Applied Optics, **63**(20), 2024: 5411-5420. https://doi.org/10.1364/AO.529070

[7] JUAREZ J.C., MAIER E.W., CHOI K.N., TAYLOR H.F., *Distributed fiber-optic intrusion sensor system*, Journal of Lightwave Technology, **23**(6), 2005: 2081-2087. https://doi.org/10.1109/JLT.2005.849924

[8] PAN Z.Q., LIANG K.Z., YE Q., CAI H.W., QU R.H., FANG Z.J., *Phase-sensitive OTDR system based on digital coherent detection*, Proceedings of SPIE, Vol. 8311, Optical Sensors and Biophotonics III, 2011: 83110S. https://doi.org/10.1117/12.905657

[9] CHENG L., PAN P., SUN Y., ZHANG Y., CAO Y., *A distributed fibre optic monitoring method for ground subsidence induced by water pipeline leakage*, Optical Fiber Technology, **81**, 2023: 103495. https://doi.org/10.1016/j.yofte.2023.103495

[10] WU H., QIAN Y., ZHANG W., TANG C., *Feature extraction and identification in distributed optical-fiber vibration sensing system for oil pipeline safety monitoring*, Photonic Sensors, **7**, 2017: 305-310. https://doi.org/10.1007/s13320-017-0360-1

[11] LINDSEY N.J., MARTIN E.R., DREGER D.S., FREIFELD B., COLE S., JAMES S.R., BIONDI B.L., AJO-FRANKLIN J.B., *Fiber-optic network observations of earthquake wavefields*, Geophysical Research Letters, **44**(23), 2017: 11,792-11,799. https://doi.org/10.1002/2017GL075722

[12] DING Z., WANG S., KANG J., ZHAO C., ZHANG Y., *Distributed acoustic sensing-based weight measurement method*, Journal of Lightwave Technology, **42**(9), 2024: 3454-3460. https://doi.org/10.1109/JLT.2024.3358490

[13] HUANG N.E., SHEN Z., LONG S.R., WU M.C., SHIH H.H., ZHENG Q., YEN N.C., TUNG C.C., LIU H.H., *The empirical mode decomposition and the Hilbert spectrum for nonlinear and non-stationary time series analysis*, Proceedings of the Royal Society A: Mathematical, Physical and Engineering Sciences, **454**, 1998: 903-995. https://doi.org/10.1098/rspa.1998.0193

[14] DRAGOMIRETSKIY K., ZOSSO D., *Variational mode decomposition*, IEEE Transactions on Signal Processing **62**(3), 2014: 531-544. https://doi.org/10.1109/TSP.2013.2288675

[15] AN X., PAN L., ZHANG F., *Analysis of hydropower unit vibration signals based on variational mode decomposition*, Journal of Vibration and Control, **23**(12), 2017: 1938-1953. https://doi.org/10.1177/1077546315605240

[16] MAHGOUN H., CHAARI F., FELKAOUI A., *Detection of gear faults in variable rotating speed using variational mode decomposition (VMD)*, Mechanics & Industry **17**(2), 2016: 207. https://doi.org/10.1051/meca/2015058

[17] MIAO Y., ZHANG B., LI C., LIN J., ZHANG D., *Feature mode decomposition: New decomposition theory for rotating machinery fault diagnosis*, IEEE Transactions on Industrial Electronics **70**, 2023: 1949-1960. https://doi.org/10.1109/TIE.2022.3156156

[18] MCDONALD G.L., ZHAO Q., MING J.Z., *Maximum correlated Kurtosis deconvolution and application on gear tooth chip fault detection*, Mechanical Systems and Signal Processing, **33**, 2012: 237-255. https://doi.org/10.1016/j.ymssp.2012.06.010

[19] ZHAO X., WU P., YIN X., *A quadratic penalty item optimal variational mode decomposition method based on single-objective salp swarm algorithm*, Mechanical Systems and Signal Processing, **138**, 2020: 106567. https://doi.org/10.1016/j.ymssp.2019.106567

[20] SOWMYA R., PREMKUMAR M., JANGIR P., *Newton-Raphson-based optimizer: A new population-based metaheuristic algorithm for continuous optimization problems*, Engineering Applications of Artificial Intelligence, **128**, 2024: 107532. https://doi.org/10.1016/j.engappai.2023.107532

Received April 21, 2025
in revised form July 6, 2025